Biomedicine & Pharmacotherapy 180 (2024) 117605

Contents lists available at ScienceDirect

Biomedicine & Pharmacotherapy

journal homepage: www.elsevier.com/locate/biopha

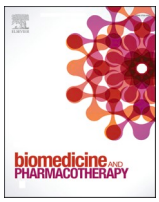

# Fully human monoclonal antibody targeting the cysteine-rich substrate-interacting region of ADAM17 on cancer cells

Nayanendu Saha [a,*], Sang Gyu Lee [b], Eeva-Christine Brockmann [c], M. Jason de la Cruz [a], Yehuda Goldgur [a], Rachelle P. Mendoza [d], Elisa de Stanchina [e], Tanzy M. Love [f], Josh Marvald [f], Yan Xu [g], Kai Xu [g], Juha P. Himanen [a], Urpo Lamminmäki [c], Darren Veach [b], Dimitar B. Nikolov [a,*]

[a] Structural Biology Program, Memorial Sloan Kettering Cancer Center, New York, NY 10065, United States
[b] Department of Radiology, Memorial Sloan Kettering Cancer Center, New York, NY 10065, United States
[c] Department of Life Technologies, University of Turku, Turku, Finland
[d] Department of Pathology and Cell Biology, Columbia University Irving Medical Center, New York, NY 10032, United States
[e] Antitumor Assessment Facility, Memorial Sloan Kettering Cancer Center, New York, NY 10065, United States
[f] Department of Biostatistics and Computational Biology, University of Rochester Medical Center, 601 Elmwood Avenue, Rochester, NY 14642, United States
[g] Texas Therapeutic Institute, Institute of Molecular Medicine, University of Texas Health Science Center at Houston, Houston, TX 77030, United States

ARTICLE INFO

*Keywords:*
ADAM17
Monoclonal antibody
Cryo-electron microscopy
Epidermal growth factor
Xenograft
Positron emission tomography

ABSTRACT

ADAM17 sheds EGFR/erbB ligands and triggers oncogenic pathways that lead to the progression of solid tumors. We targeted the ADAM17 disintegrin and cysteine rich domain region (D+C) to generate a panel of single-chain antibody fragments (scFvs) that selectively bind to the D or C domains of ADAM17, but not of ADAM10 or ADAM19. From the panel, we selected one scFv, referred to as C12, based on its high binding affinity towards the target, and re-formatted it to a full IgG for further studies. High-resolution cryo-electron microscopy studies documented that the mAb binds to the ADAM17 C-domain that in ADAM proteases, notably ADAM10 and ADAM17, is known to impart substrate-specificity. The C12 mAb significantly inhibited EGFR phosphorylation in cancer cell lines by hindering the cleavage of EGFR ligands tethered to the cell surface. This inhibition provides a mechanism for potential anti-tumor effects, and indeed C12 diminished the viability of a variety of EGFR-expressing cancer cell lines. Cell-based ELISA studies revealed that C12 preferentially bound to activated ADAM17 present on tumor cells, as compared to the autoinhibited ADAM17 that is the predominant form on HEK293 and other non-tumor cells. C12 also exhibited tumor growth inhibition in an ovarian cancer xenograft mouse model. Consistent with its selective tumor cell binding in vitro, radioimmuno PET (positron emission tomography) imaging with $^{89}$Zr-DFO-C12 in mouse xenograft models confirmed tumoral accumulation of the C12 mAb.

## 1. Introduction

Identification of targeted therapies is an urgent task in cancer research [1]. Dysregulated signaling by EGFR/erbB receptor tyrosine kinase family members leads to the progression of a wide variety solid tumors such breast, ovarian and non-small cell lung cancer [2–6]. EGFR/ErbB ligands are cleaved from the cell surface by the metalloprotease ADAM17, which is activated in solid tumors, initiating the signaling that drives tumor growth and proliferation [7]. Since ADAM17 plays a key role in multiple oncogenic pathways, it is reasonable to anticipate that ADAM17 inhibition could be used as a therapy for a broad patient population [8,9]. ADAM proteases consist of an N-terminal pro-sequence followed by metalloprotease (M), disintegrin (D), cysteine-rich (C, also referred to as membrane proximal domain or MPD [17]), transmembrane and cytoplasmic domains [10,18]. The D and C domains have been shown to bind ADAM substrates and dictate substrate specificity [11–13]. While ADAM17 is a well validated target, small molecule inhibitors against its active site in the M domain failed clinical trials due to lack of specificity, efficacy, and toxicity issues [14,15].

* Corresponding authors.
*E-mail addresses:* sahan@mskcc.org (N. Saha), nikolovd@mskcc.org (D.B. Nikolov).

https://doi.org/10.1016/j.biopha.2024.117605
Received 8 August 2024; Received in revised form 5 October 2024; Accepted 21 October 2024
Available online 25 October 2024

Previously, we reported the generation and characterization of an affinity-matured fully human monoclonal antibody (mAb), D8P1C1, that selectively recognizes ADAM17 on cancer cells by preferentially binding to an activated ADAM17 conformation present on cancer cells (v.s the housekeeping/autoinhibited conformation present on most non-cancer cells) [16]. D8P1C1 inhibited cancer progression both in vitro and in pre-clinical settings, by binding to and inhibiting substrate access to the catalytic (M) domain [16]. In this study, we pursue an alternative ADAM17 targeting strategy, based on our previous characterization of a substrate-recognition motif within the D+C domain region in ADAM proteases [12]. To that end, we generated a mAb, named C12, that binds to the C-domain (a.k.a. MPD) of ADAM17. Our goal was to investigate the anticancer effect of this mAb in vitro and examine ADAM17-targeted molecular imaging in preclinical settings. The mAb exhibited moderate anti-tumor efficacy in vitro and in vivo. C12 bound selectively to activated ADAM17 present on cancer cells and accumulated in tumors in PET-based imaging studies. Although the therapeutic potential of the C12 mAb as a single agent was not pronounced, we envisage that it can be used as a scaffold to develop antibody-based therapeutics because of its ability to selectively target tumor cells and its much lower toxicity profile than small-molecule strategies.

## 2. Materials and methods

### 2.1. Cell lines

The triple-negative breast cancer (TNBC) cell line MDA-MB-231 and the non-high grade serous ovarian cancer cell line SKOV-3 were cultured in Dulbecco's Modified Eagle Medium (DMEM), 10 % Fetal Bovine Serum (FBS), 1 % Penicillin/Streptomycin (P/S) and 2 mM L-Glutamine. The HER2 positive SKBR-3, the colon cancer lines HT-29/HCT116 and clear cell ovarian cancer line ES-2 were grown in McCoy's 5a, 10 % FBS and 1 % P/S. high-grade serous ovarian (HGSOC) cell line OVCAR-3 was cultured in RPMI-1640, 10 % FBS, 1 % P/S, 10 mM HEPES and 0.2 units/ml Insulin. The lung adenocarcinoma cell line HCC-827 and the colon cancer line COLO205 were cultured in RPMI-1640, 10 % FBS and 1 % P/S. The endometroid ovarian cancer cell line TOV112D was grown in ATCC formulated 1:1 MCDB 105 media containing a final concentration of 1.5 g/L sodium bicarbonate and Medium 199 containing a final concentration of 2.2 g/L sodium bicarbonate, 10 %FBS. These cell lines were purchased from American Type Culture Collection (ATCC). The LIM1215 colon cancer cell line (Cell Bank Australia) was cultured in RPMI1640 with 2 mM L-Glutamine, 25 mM HEPES, 10 % FBS, 0.6 μg/ml Insulin, 1 μg/ml Hydrocortisone and 10 μM Thiolglycerol [19]. The cell lines were regularly tested for mycoplasma contamination and sub-cultured according to the instruction manual.

### 2.2. Generation of C12 mAb

The human ADAM17 construct 474–646, encompassing the D+C domains, was cloned in a custom-made pMA152a baculovirus vector. The secreted protein fused to a removable C-terminus Fc tag, was produced in baculovirus-infected Hi5 insect cells. The Fc tagged protein was purified through protein A Sepharose and upon cleavage of the Fc-tag, the final round of purification was performed on SD-200 size-exclusion chromatography (SEC), GE Biosciences [16]. ADAM17(D+C) binders were generated by interrogating synthetic single chain antibody fragment (scFv) phage libraries scFvP and scFvM with using phage display, as described before Huovinen et al. [20]. The antigen, ADAM17 (D+C), was biotinylated with EZ-LinkNHS-PEG4-Biotin (Thermo scientific, USA) and immobilized on Dynabeads M280 streptavidin beads (Invitrogen, Norway). On the 1st phage display panning round, 2.4 μg of biotinylated ADAM17(D+C) immobilized on 0.3 mg of beads were incubated for 1 h with $4\times10^{12}$ cfu scFvM and scFvP library phages mixed in 1:1 ratio in 4 ml of TBT-0.05 buffer (50 mM Tris-HCl pH 7.5, 150 mM NaCl, 1 % bovine serum albumin, 0.05 % Tween 20). Beads were then washed four times followed by elution of the bound phages with trypsin. *E.coli* XL1-Blue cells were infected with the eluted phages. After infection, new phage stocks were produced in liquid cultures with help of VCS M13 helper phage. On the subsequent panning rounds $1\times10^{11}$ cfu of phages were mixed in a 1 ml reaction with 0.05 mg of beads coated with 0.6 μg of biotinylated ADAM D+C. In total, three rounds of phage display selection were carried out and enrichment of specific phages was monitored by phage immunoassay. Finally, the enriched scFv genes from the second and third panning rounds were excised from the phagemid vector by *Sfi*I and cloned as a pool in pLK06H vector [20] where the scFvs were genetically fused to bacterial alkaline phosphatase (AP). The vector pool was used to transform *E. coli* XL1-Blue cells, followed by lifting single colonies and growing them in 96 well format for single clone immunoactivity screening [20]. The activities of the scFv-AP fusion proteins expressed, were evaluated by Enzyme linked Immunosorbent Assay (ELISA) using biotinylated ADAM17(D+C) immobilized on Streptavidin coated microtiter plates (Uniogen, Finland). The genes of the selected scFv antibody clones were re-cloned at *Sfi*I sites in His-FLAG-pEB06 vector [20]. The scFvs containing a Histidine- and a FLAG-tag were produced in *E. coli* and purified using Nickel-NTA resin (Thermo Scientific, USA).

### 2.3. Alamar blue cell viability assay

The cancer cells were harvested in the log phase of growth, adjusted to $5\times10^4$ cells/ml, and plated in 96-well cell culture plates. The cells were grown for 24 h, treated with C12 mAb in varying concentrations, and allowed to grow for additional 36–38 hours. Cells not treated with the mAb were used as a control. Alamar Blue (Bio-RAD Laboratories) (10 % of the well volume) was added aseptically and incubated for 6 h. Cell viability was measured spectrophotometrically by absorbance at 570 and 600 nm. Cell viability was calculated using the following formula:

Percentage difference between treated and control cells
= ((O2 x A1) - (O1x A2) X 100)/((O2 x P1) – (O1 x P2))

O1 = molar extinction coefficient (E) of oxidized alamarBlue® (Blue) at 570 nm, O2 = E of oxidized alamarBlue® at 600 nm, A1 = absorbance of test wells at 570 nm, A2 = absorbance of test wells at 600 nm, P1 = absorbance of growth control well (cells plus alamarBlue® but no test agent) at 570 nm, P2 = absorbance of growth control well (cells plus alamarBlue® but no test agent) at 600 nm [21].

### 2.4. Fluorescent peptide cleavage assay

For this assay, we expressed and purified the ectodomain (ECD) of human ADAM17(20−642) from baculovirus-infected Hi5 insect cells, as was described above for the ADAM17(D+C) construct. The mAbs C12, as well as a Fab fragment derived from C12 IgG by papain digestion, were buffer-exchanged into 25 mM Tris, pH 9.0, containing 2 μM ZnCl2, and 0.005 % (w/v) Brij-35. For comparison, we included the previously reported anti-ADAM17 mAb D8P1C1 [16] in our assay. ADAM17-antibody complexes were formed at a 1:1 molar ratio prior to the assay. The assay was carried out by mixing 50 μM of a fluorogenic peptide substrate Mca-PLAQAV-Dpa (R&D Systems Cat# ES003) [15,16] with ADAM17-antibody complexes at 37°C and monitoring the progress of the enzymatic reaction by fluorometrically (excitation 320 nm and emission 405 nm) over a time course of 1 h. ADAM17-ECD alone was used as a positive control [22,23].

### 2.5. Cell-based ELISA assays to gauge the binding of anti-ADAM17 mAb C12 to cancer cell lines

Cellular ELISA [24] was performed as described before [16] to gauge the binding of the anti-ADAM17 mAb C12, relative to the binding of the MED13622 mAb, to ADAM17 expressed on the cell surface of cancer cell lines (breast, ovarian, colon, adenocarcinoma), as well as to HEK293

cells and HEK293 cells transfected with full-length human ADAM17. Briefly, $5\times10^4$ cells/well were immobilized on 96-well ELISA plates (Greiner bio-one) with 1 % paraformaldehyde for 2hrs at $37^0$ C. The plate was washed thrice with PBS and blocked for 2 hrs at room temperature with 4 % non-fat dry milk. The anti-ADAM17 mAbs (C12 or MED13622) were added in varying concentrations and binding was detected using mouse mAb conjugated to HRP and recognizing human IgG. Color was developed using the TMB substrate kit (Thermo Scientific). The data was recorded at 450 nm.

### 2.6. In vivo antitumor efficacy studies

SKOV-3 cells were grown in monolayer culture, harvested by trypsinization, and implanted subcutaneously into the right flank of 6- to 8-week-old female NSG mice. Approximately 10 million cells (SKOV-3) were injected per mouse. Mice were randomized into 5 mice per group. When tumors reached 100 $mm^3$, the anti-ADAM17 mAb C12 (40 mg/kg) was injected intraperitoneally (i.p.) twice a week for four weeks. The chemotherapeutic agent paclitaxel, (15 mg/kg) was diluted in saline prior to treatment, so that injection volume is 500 μl. Paclitaxel was administered intravenously (i.v.) once a week for first three weeks. For combination assay with C12, the chemotherapeutic agent was injected one day after the administration of the mAb. Sterile PBS was used as a control. Tumor volume was determined as described before [16]. Antitumor efficacy was calculated as (1-dT/dC) X100, where dT is the final tumor volume minus the starting tumor volume from the treatment group and dC is the final tumor volume minus the starting tumor volume of the control group [25]. Error bars were calculated as SEM. The mouse body weight and general health were monitored daily, and the experiments were carried out in accordance with Association for Assessment and Accreditation of Laboratory Animal Care and MSKCC Institutional Animal Care and Use Committee guidelines.

### 2.7. Sandwich ELISA to quantitate endogenous levels of total EGFR and EGFR-P (phosphorylated EGFR) in lysates of MDA-MB231, HCC-827 and SKOV-3 cells untreated and treated with C12

The cancer cells were harvested in the log phase of growth, adjusted to $5\times10^4$ cells/ml, and allowed to adhere and grow for 24 h in 24-well cell culture plates (Greiner bio-one Cellstar). The cells were treated with 10 μg/ml of C12 mAb and harvested after 4 h of treatment. Pathscan sandwich ELISA kits were used to measure total EGFR/erbB and EGFR-P at the in treated and untreated cells [26]. We employed the manufacturers protocol (Cell signaling technology). Briefly, the cells harvested after 4 h and resuspended in 1X lysis buffer containing 1 mM PMSF, sonicated on ice and centrifuged for 10 min (x14,000 rpm) at 4°C. The supernatant, which is the cell lysate was used for further study. We added 100 μl of the lysates (diluted to 1 mg/ml) to the microwells. The wells were coated with a mouse mAb to EGFR, that captures both phosphorylated and non-phosphorylated EGFR. An anti-EGFR mAb raised in rabbit was used to detect the bound EGFR. The EGFR-P phosphorylated at Tyr1068 was detected by anti-phospho-EGF receptor (Tyr1068) mAb raised in rabbit. HRP-linked anti-rabbit antibody was used in both cases to recognize the bound antibody (detection antibody). Color was developed using the TMB substrate. The data was recorded at 450 nm. Lysates from untreated cells served as controls. Comparison of EGFR and EGFR-P levels between treated and untreated groups was performed using independent t test.

### 2.8. Sandwich ELISA to quantitate the cleavage of EGFR ligands (EGF, Amphiregulin or AREG, TGFα) and other ADAM17 substrates (TNFα, CX3CL1, Notch) from cancer cell lines untreated and treated with C12

The cancer lines (MDA-MB-231, HCC-827, OVCAR-3 and CaOV-3) were harvested in the log phase of growth and allowed to adhere to 24-well cell culture plates (Griener bio-one cell star). The cells were treated with 20 μg/ml C12 mAb or 1 μM small-molecule inhibitors of ADAM10 (GI254023X) [27], ADAM17 (TAPI-1) [28] or of Matrix metalloprotease or MMPs (Batimastat) [29], for 24 h. The supernatants of treated and untreated cells were harvested and subjected to sandwich ELISA (Invitrogen). Briefly, ligands or substrates shed in the supernatants were bound to wells coated with corresponding capture antibodies. Human ADAM17-substrate biotin conjugates were added, followed by Streptavidin HRP. Color was developed using TMB. For the substrate Notch, the effect of C12 on regulated intramembrane proteolysis (RIP) was evaluated and the release of Notch ICD in the lysates was measured. To detect NICD1, PathScan® cleaved Notch1 (Val1744) sandwich ELISA Kit (Cell Signaling Technologies) [30] was used. The data was recorded at 450 nm.

### 2.9. CryoEM sample preparation, data collection, and structure determination

A 1:1 mix of ADAM17-ECD and C12 Fab at a final concentration of 5 μM was incubated on ice for 30 min. 3 μl of the sample was applied to glow-discharged QUANTIFOIL R1.2/1.3 Au 400 mesh grids (Quantifoil Micro Tools GmbH, Jena, Germany), blotted for 4 s, and plunge-frozen in liquid ethane using a Vitrobot Mark IV (Thermo Fisher Scientific Inc., Hillsboro, OR, USA). Data was collected using a Titan Krios G2 (Thermo Fisher Scientific) transmission electron microscope operated at 300 kV with sample chamber at liquid nitrogen temperature. Images were recorded with a Gatan K3 direct detector (Gatan, Inc., Pleasanton, CA, USA). Using the SerialEM program for automated data collection, 4473 total exposure movies were collected in super-resolution mode, at a raw pixel size of 0.41275 Å $px^{-1}$ and 65.9 e− $Å^{-2}$ total dose. A beam-image shift procedure [31] in SerialEM was used to quickly collect data on individual QUANTIFOIL holes in a 3×3 array per exposure target. The defocus range for the collection was −1.0 to −2.5 μm.

Datasets were processed using CryoSPARC [32] version 4.4.0. CryoSPARC's implementation of patch motion correction was used to Fourier-crop the raw data to a pixel size of 0.8255 Å $px^{-1}$. CryoSPARC Live was employed during data collection and provided the source of the initial 2D classification run using the automated blob picking of particles with a diameter range of 50–170 Å. Manual selection of 2D classes provided the templates for template picking during the Live session, which yielded 800,174 particles from 1174 micrographs. With these particles, an initial model was used to bootstrap the 3D structure using the heterogeneous refinement jobtype. 2D templates were created and used by the automated template picker to pick particles with a diameter of 170 Å, using 3093 micrographs curated from the 4473 total exposures of the complete dataset. Following inspection of the particles, 1898,088 particles were extracted at a box size of 384 px and binned by 3. These particles were split into 200 classes by 2D classification, then manually selected into two groups for refinement: a group of "pristine" 2D classes for a consensus refinement, and a group of "bad" classes containing particles that did not correspond to the sample. "Pristine" classes contained images of the Fab antibody at different orientations. Both groups were made into 3D volumes via the ab-initio reconstruction routine.

Heterogeneous refinement was employed to filter the "pristine" particles from the "bad" particles in an iterative way, using the previous output particles as input. Heterogeneous refinement uses a 3D volume-based classification method to group the 2D particles into 3D volumes specified as input. For filtering the "bad" classes out of the dataset, two of the input volumes for heterogeneous refinement consisted of a duplicated ab-initio volume of the "pristine" 3D class, and four input volumes were from the ab-initio volumes of the "bad classes". 5 successive rounds of heterogeneous refinement from the original inputs above yielded 311,930 particles. These particle images were unbinned to the original 384-px box size, then refined to 3D against the most recent 3D volume from the last heterogeneous refinement job using the non-uniform refinement routine, yielding a map at 3.24 Å resolution. The particles from this map were used to produce two low-pass filtered

maps at 15 Å. One of these maps went on to create templates for picking more particles from the 3093 micrographs, via ab-initio splitting of the data into 4 classes, and a duplication of the data with manual selection of 2D particle images via 2D reconstruction. Both duplicate attempts to accumulate more particles used 5 rounds of successive heterogeneous refinements each to refine particles against the best 3D map. Another heterogeneous refinement job was used to combine the particles, and duplicate particles were subsequently removed, yielding 438,366 particles. A non-uniform 3D refinement of these particles generated a map with 3.15 Å resolution.

In an attempt to improve the resolution, this map was segmented using the molecular modeling software UCSF Chimera [33] version 1.17.1. Masks of the head and tail regions of the particle were generated by RELION [34] version 3.0.8. Coordinates of the "fulcrum" (pivot point at which the head and tail meet) were also identified in Chimera and used in multiple rounds of 3D local refinement in CryoSPARC. However, there was no discernible improvement in the map resolution after these final refinements.

#### 2.9.1. Image processing, model building, and refinement

The model of the antibody was generated using ABodyBuilder-ML developed by the Oxford Protein Informatics Group (OPIG) [35]. It was fit into cryoEM map using Phenix [36]. The ADAM17 model was based on PDB entry 2AO7 and was fit into the map manually. Interactive model building was performed using O [37]. Real space refinement was done with Phenix [38].

### 2.10. Radiochemistry, PET imaging and ex vivo biodistribution

The anti-ADAM17 mAb C12 was buffer exchanged into HEPES buffer (pH 8.5, 0.5 M) and conjugated with deferoxamine (DFO) using 5 molar equivalents of *p*-SCN-DFO (10 mM in DMSO, B-705, Macrocyclics Inc., Plano, TX). The conjugation reaction was incubated at 37 °C for 90 min, then purified by PD10 Sephadex G25 gel filtration chromatography (Cytiva Life Sciences, Marlborough, MA) in 0.5 M HEPES (pH 7.5) to yield DFO-C12 at a concentration of 1–2 mg/ml. For radiolabeling, $^{89}$Zr-oxalate in 1 M oxalic acid (3D Imaging LLC, Little Rock, AR) was neutralized to pH 7 using 2 M $K_2CO_3$ by narrow-range pHydrion paper (Micro Essential Laboratory, Inc., Brooklyn, NY) followed by addition of DFO-C12, then incubated at room temperature for 90 min. Radiolabeling progress, radiochemical purity of the purified $^{89}$Zr-DFO-C12 and stability in PBS and mouse plasma at 37°C was assessed by radio-instant TLC (thin layer chromatography) on iTLC-SG paper (Agilent Technologies, Inc., Santa Clara, CA) in an aqueous solution of DTPA (10 mM, pH 5) read using an AR2000 scanner (Bioscan, Inc., Washington, DC) [39]. The measurements were determined using a radio-instant TLC Scanner. $^{89}$Zr-DFO-C12 was purified by PD10 gel filtration chromatography (equilibrated in normal saline), and sterile filtered prior to in vivo imaging and biodistribution studies. MAbs were also analyzed using size-exclusion HPLC with radiodetection (TSKgel® UP-SW3000, 15 cm×4.6 mm, 0.25 ml/min, 0.4 M $NaHClO_4$, 0.05 M $Na_2HPO_4$, pH 6). NSG mice were inoculated with $10\times10^6$ OVCAR3 or $5\times10^6$ SKOV3 cells on the right flank of the mice (n=3). Nine days after inoculation, $^{89}$Zr-DFO-C12 (50 μg, 3MBq (80μCi) in 250 μL) was administered intravenously by tail vein. microPET/CT imaging was performed on an Inveon (Siemens Medical Solutions) at 24 h, 72 h, and 168 h. PET/CT visualization, segmentation, and region-of-interest (ROI) analysis was performed using Amide 1.0.6 [40] and represented as percent of injected dose per cc (assumed 1 cc = 1 g) of tissue (%ID/g). For ex vivo biodistribution, tissues were dissected, weighed and radioactivity concentrations determined by measurement in a γ-well counter (Hidex AMG, Turku, Finland), represented in terms of %ID/g, and plotted using Prism 10 (GraphPad Software, Boston, MA).

### 2.11. Statistical analysis

The data from all in vitro and cell-based assays described, including Alamar blue, fluorescent peptide cleavage and ELISA-based assays, are representative of triplicate determinations and two independent experiments. Statistical analysis was performed using IBM SPSS version 29. P values were calculated using either one-way ANOVA with a Dunnett's multiple comparison post hoc test, or one- or two-tailed independent t test analysis as indicated on each figure. A p value of $< 0.05$ was considered significant.

## 3. Results

### 3.1. Generation and purification of the C12 mAb

We used phage display to isolate binders against ADAM17 from large synthetic antibody libraries, where human immunoglobulin genes are displayed as a single chain antibody fragment (scFv) on filamentous phage [20]. The antigen used for the antibody generation was the human ADAM17 D+C domain region. After the second and third phage display enrichment rounds, the antibody genes were sub-cloned and expressed as soluble fusion proteins to alkaline phosphatase (scFv-AP). Binding properties of the individual antibody clones were assessed using immunoassays resulting in 24 out of 33 and 38 out of 39 selected clones showing specific binding to ADAM17 D+C after the second and third panning rounds, respectively. By sequencing of 30 clones, 14 unique sequences were identified. The unique antibody clones (binders) were re-cloned in His-FLAG-pEB06 vector [20] as a scFv-His-FLAG fusion. All 14 binders were purified from *E. coli* using Nickel-NTA resin. Based on binding affinity, we selected the C12 binder and reformatted it to a fully human IgG using human $IgG_1$ sequences for the constant regions. The C12 mAb was subsequently purified to ≥99 % homogeneity using protein A Sepharose followed by SEC-HPLC. On SDS-PAGE, under non-reducing conditions C12 migrated at 150 kDa. Under reducing conditions, the heavy and light chains migrated at 50 and 25 kDa respectively (Fig. S1). In ELISA-based assay C12 specifically recognized human and mouse ADAM17(D+C) and not human or bovine ADAM10 (D+C) or human ADAM19(D+C) (Fig. S2). C12 bound to the ADAM17 (D+C) and ADAM17(ECD) protein constructs with a $K_D$ of ~25 nM and ~60 nM respectively on Biolayer Interferometry (BLI) (data not shown).

### 3.2. Structure of C12 bound to ADAM17

We determined the high-resolution cryo-EM structure of the C12 Fab in complex with the D+C domain region of ADAM17, which is shown on Fig. 1A. The structure reveals that C12 interacts only with the C domain of ADAM17, utilizing residues of both the light and the heavy mAb chains. Our previous structure-function studies on ADAM proteases highlighted the importance of the D+C region for substrate-recognition [12,13]. We also previously characterized a conformation-specific antibody, 1H5, which bound the C domain of the related metalloproteinase ADAM10 [41]. The conformation specificity of 1H5 was due to the fact that it bound the concave face of the D+C region in a way that it partially overlapped with the position of the M domain in the autoinhibited ADAM10 conformation, thus making it specific for the activated ADAM10 conformation. C12, on the other hand, binds the C domain [18] or MPD [17] of ADAM17 at the convex side of the L-shaped D+C region. Therefore, C12 would not directly interfere with the conformational rearrangements and movements of the M domain of ADAM17, and the reason for its conformation specificity is not the same as in the case of 1H5 [41]. The heavy chain of C12 Fab interacts with the CXCC motif, the conformation of which has been suggested to be different in the activated and autoinhibited ADAM proteases [41,42], and this could be a plausible explanation for the selectivity of C12 for activated ADAM17 (Fig. 1A). Interestingly, our grid preparations contained a construct of the complete ADAM17 ectodomain, but only the

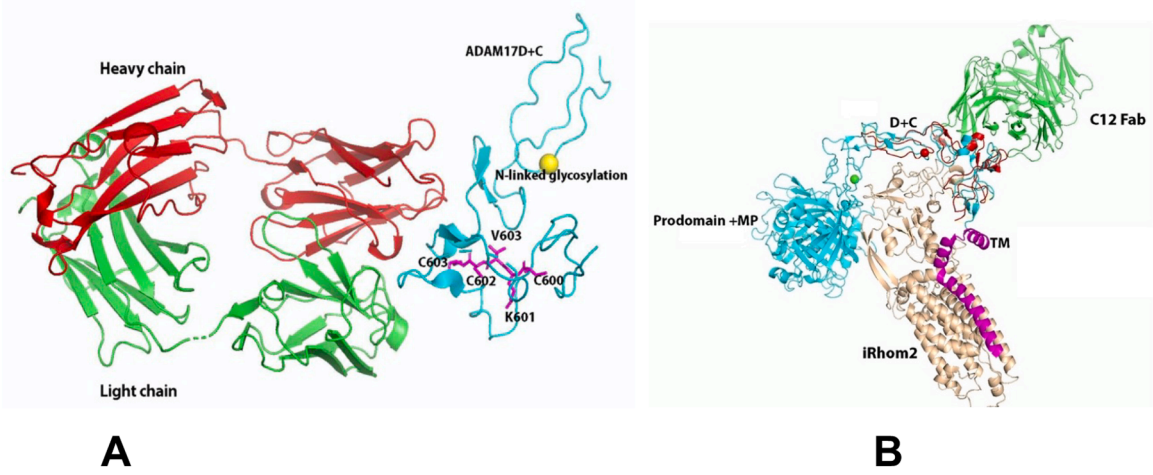


**Fig. 1.** (**A**) Structure of the complex between the C12 Fab (colored in red and green) and the D+C region of ADAM17 (colored in cyan). Highlighted is the position of the bound C12 relative to the CxxCC motif (colored in magenta). (**B**) The D+C domains of ADAM17 (colored in red) bound to the C12 Fab (colored in green) aligned to the D+C region of the ADAM17 ectodomain (colored in cyan and including the prodomain) bound to iRhom2 [43] (colored in gold).

D+C region was visible in the calculated maps, suggesting that there is high flexibility in the connection between the MP domain and the D+C domains resulting in a variety of ADAM17 conformations that cannot be easily averaged into individual structures. This agrees with the recently published structure of the mature ADAM17 ectodomain in complex with iRhom2 [43], an ADAM17 regulatory protein, where the authors were also unable to locate the MP domain due to high degree of flexibility [43]. The structure of the D+C region in the complex with C12 is very similar to the structure of the D+C region in the ADAM17-ECD that contains the prodomain (pdb id: 8SNL) [43] (and these are also similar to the structure of the ADAM10 D+C region [12]). The RMSD between the N-terminal first 60 amino acids of the D+C regions is 1.804 Å while that between the remaining C-terminal regions is 1.342 Å (Fig. 1B). The structure alignment on Fig. 1B also indicates that C12 will be able to bind ADAM17 when it is in complex with iRhom2 as the two molecules bind different sides of the ADAM17 D+C region.

### *3.3. C12 does not inhibit the enzymatic activity of ADAM17 towards small substrates*

To evaluate the effect of C12 on the enzymatic activity of ADAM17, we performed a peptide cleavage assay as previously described [16]. This assay (Fig. 2) clearly showed that the C12 mAb or its Fab fragment, unlike the D8P1C1 mAb [16] (which binds to the protease domain), was ineffective in preventing the cleavage of small peptides. This is because C12 binds to the convex side of the C domain and does not impair access of small-peptide substrates to the M domain.

### *3.4. C12 inhibits the shedding of EGFR ligands with similar efficiency, but with varying efficiency for other ADAM17 substrates*

As C12 binds the ADAM17 D+C region, which is known to mediate interactions with cell-surface protein substrates [18,43], we next evaluated how the mAb affects the shedding of physiological ADAM17 substrate from the surface of live cancer cells. First, we selected cancer cell lines that express EGFR ligands, including EGF, TFGα, AREG, and carried out sandwich ELISA-based shedding assays (Invitrogen) to quantify the release of these EGFR ligands into the cell culture supernatant or plasma. It is known that ADAM17-dependent shedding of TGFα and EGF promotes invasion and cell migration of TNBC (MDA-MB231 cells) [44,45]. Likewise, EGF, TGFα and TGFβ modulate cell growth of ovarian cancer cells (OVCAR-3, CaOV-3) [46]. Elevated AREG levels are known to upregulate genes associated with the immune invasion of HGSOC ovarian cancer cells (OVCAR-3, CaOV-3) [47].

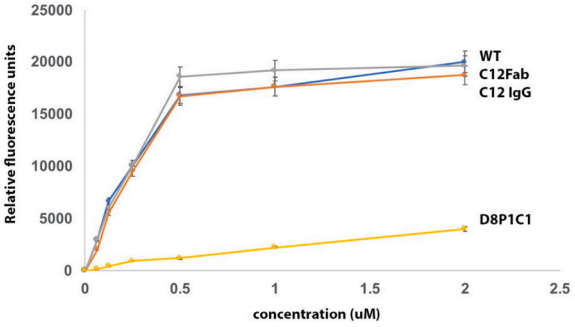


**Fig. 2.** FRET-based peptide cleavage assays. The data shows that C12 IgG or Fab do not inhibit cleavage of short peptides derived from TNF alpha. For comparison we included the anti-ADAM17 mAb D8P1C1, which binds to the protease domain and efficiently inhibits the cleavage of these peptides. The data represent mean of triplicate determinations and two independent experiments (mean fluorescence ± SEM). Maximum dispersion was within 10 % of the mean value. Proteolytically active human ADAM17-ECD/antibody complexes were formed at 1:1 molar ratio prior to the assay, which was carried out in the presence of 50 μM of a fluorogenic peptide as described in the Materials and Methods section. Statistical analysis revealed significant decrease in peptide cleavage (fluorescence) between the D8P1C1 treated and untreated ADAM17 samples ($p<0.001$, one way ANOVA with a Dunnett's multiple comparison post hoc test). Treatment with the C12 IgG or C12 Fab, on the other hand, did not significantly change the peptide cleavage/fluorescence ($p>0.05$).

Second, we evaluated the shedding of other ADAM17 substrates that are not ligands for EGFR. Of these, TNFα stimulates TNBC stem cells and aids in intramural invasion [48], while the chemokine CX3CL1 abets the pathogenesis of NSCLC [49] (HCC-827). The results, shown on Fig. 3, document that C12 inhibits with similar efficiency (60 %-70 % inhibition) the shedding of all EGFR ligands in all cancer cell lines that were tested. For the other ADAM substrates, the inhibition varied from 64 % for TNFa, to 50 % for CX3CL1, to 4 % for Notch1. It should be noted that the small-molecule ADAM17 inhibitor TAPI-1, which binds to the proteinase active site, was somewhat more efficient in blocking shedding than the C12 mAb under all conditions. In addition, none of the ADAM17 antagonists had any significant effect on Notch RIP [30], which could be attributed to ADAM10, and not ADAM17, being the primary Notch1 sheddase in these cells [50].

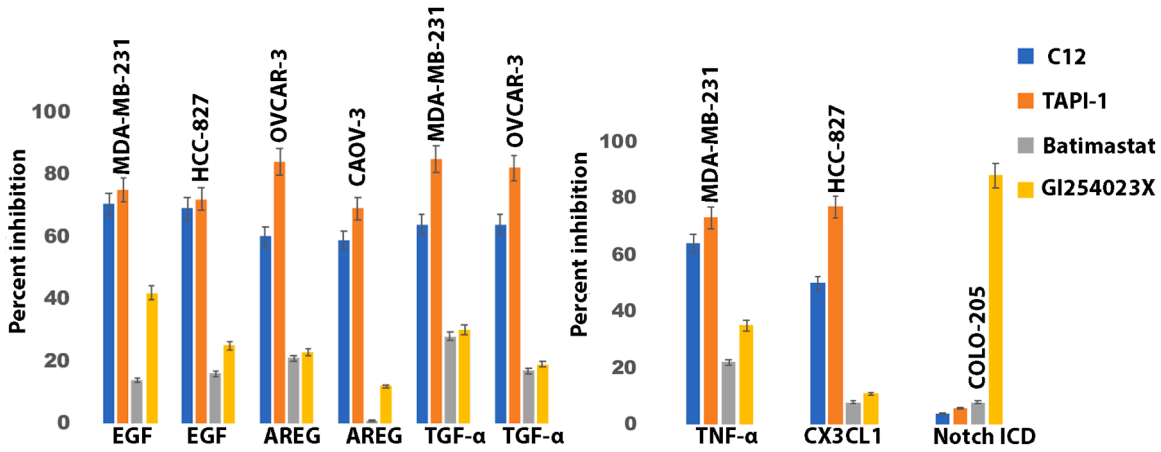


**Fig. 3.** C12 inhibits the shedding of EGFR ligands and other ADAM17 substrates on the cell surface. Sandwich ELISA was employed to quantitate the shedding or cleavage of EGFR ligands (**A**) and other ADAM17 substrates (**B**). For Notch, we measured the release of the Notch intracellular domain or NICD1 in the cell lysates. Percent inhibition of shedding by the antagonists was calculated by measuring the decrease in shedding observed in comparison to the untreated wells. The data represent mean of quadruplicate determinations and the bars show the effect of administration of antagonists on the different cancer cells (as indicated above the bars) relative to the control (untreated) mean ± SEM.

### *3.5. C12 inhibits EGFR/erbB phosphorylation in MDA-MB-231, HCC827 and SKOV-3 cells*

As mentioned above, upon shedding of EGFR/erbB ligands (EGF, TFGα, AREG), these ligands bind to EGFR/erbB receptors resulting in activation of downstream signaling, which involves receptor dimerization, autophosphorylation, internalization, and lysosomal degradation [51,52]. To evaluate the effect of C12 on EGFR/erbB phosphorylation, we selected the tumor cell lines MDA-MB-231 (breast), HCC827 (lung) and SKOV-3 (ovarian), which are known to express high levels of EGFR. We measured the levels of total EGFR and phosphorylated EGFR (EGFR-P), with or without C12 treatment, using sandwich ELISA kits (PathScan Cell signaling technologies) [26]. The results shown on Fig. 4 revealed that 4 h of incubation with C12 resulted in over 80 % inhibition of phosphorylation. It is likely that the C12 mAb affects EGFR phosphorylation by inhibiting the shedding of EGFR/erbB ligands (see Fig. 3 above) via blocking their interactions with ADAM17.

### *3.6. C12 inhibits the proliferation of multiple cancer cell lines overexpressing EGFR/HER2 and preferentially binds to ADAM17 expressed on these cancer cells as compared to HEK293 cells*

Next, we performed Alamar blue cell viability assays with the following cancer cell lines: OVCAR-3, SKOV-3, CAOV-3, ES-2, TOV112D (ovarian) and MDA-MB-23, SKBR-3 (breast), HCC-827 (non-small cell lung cancer or NSCLC). OVCAR-3, CAOV-3, SKOV-3, ES-2 and TOV112D represent different types of epithelial ovarian cancer cell lines [53]. The C12 mAb inhibited proliferation of these cell lines to varying degrees, with the serous cells (high grade and non-high grade) exhibiting 30–50 % inhibition at a C12 concentration of 20 μg/ml. However, C12 showed only nominal inhibitory effect on the clear (ES-2) and endometroid (TOV112D) cell lines (Fig. 5A). We also performed cell-binding assays, similar to those described for the anti-ADAM17 mAb D8P1C1 [16] and the anti-ADAM10 mAb 1H5 [41], in order to correlate the anti-proliferative potency of the C12 mAb with its binding preference for activated ADAM17 present on cancer cells. In ELISA cell-binding experiments (Fig. 5B) the C12/MED13622 signal ratio observed in cancer cell lines, relative to the C12/MED13622 signal ratio observed in the untransfected HEK293 cells, indicated that: (i) C12 preferentially recognizes the activated conformation of ADAM17 on cancer cell lines as opposed to the autoinhibited conformation of ADAM17 expressed on HEK293; (ii) C12 recognizes cell surface expressed ADAM17 on HGSOC and non-HGSOC cell lines more effectively, indicating that these cells display a higher ratio of activated ADAM17 compared to the endometroid and clear cell lines The enhanced binding of C12 presumably explains why it is more effective in inhibiting the proliferation of HGSOC and non-HGSOC cancer cells. The breast cancer cell lines, including the TNBC MDA-MB-231 and the HER2/erbB2-overexpressing SKBR-3, as

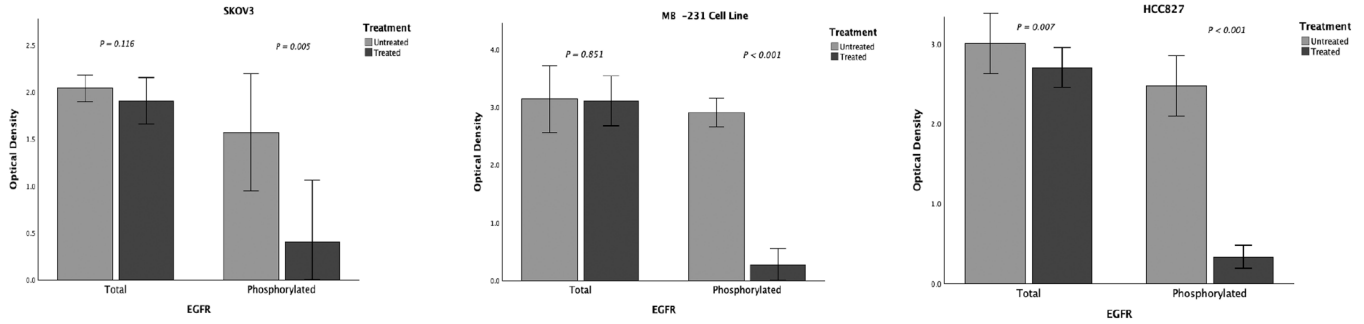


**Fig. 4.** C12 inhibits EGFR/erbB phosphorylation in cancer cells in vitro. Sandwich ELISA was used to measure the levels of total and phosphorylated EGFR (EGFR-P) in MDA-MB-231, HCC827 and SKOV-3 cells upon treatment with 10 μg/ml C12. The data represent mean of triplicate experiments, and the bar plots show the effect of treatment with C12 relative to untreated control, mean ± SEM. Comparison of EGFR levels between treated and untreated groups was performed using independent t test. Total EGFR levels did not significantly differ between the two groups in MDA-MB-231, p=0.85; SKOV-3, p=0.116. However, in HCC827, the small but statistically significant difference could be due to a decrease in the total number of viable cells. On the other hand, the mAb-treated group showed significant decrease of the EGFR-P levels in all cell types, as compared to the untreated control $p<0.001$, p=0.005.

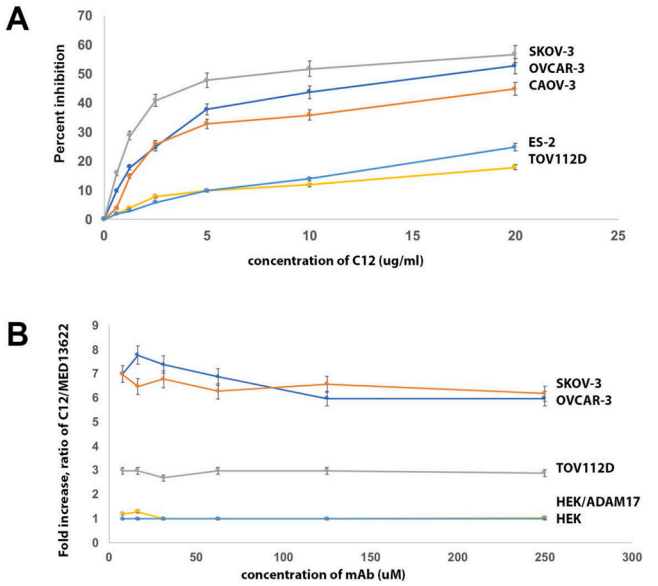


**Fig. 5.** (**A**) Alamar blue cell viability assays with ovarian cancer cell lines. Percent growth inhibition is shown for ovarian tumor cell lines (SKOV-3, CAOV-3, OVCAR-3, ES-2, TOV112D), treated with C12 IgG. The data represent mean of triplicate determinations and two independent experiments, and the plots show the effect of treatment of mAbs on cancer cells relative to the control, mean ± SEM. (**B**) C12 preferentially binds to the activated, tumor-specific conformation of ADAM17 present on ovarian cancer cells. Cellular ELISA was performed to gauge the binding of C12, relative to the binding of the control MED13622 mAb, to ADAM17 expressed on the cell surface of ovarian cell lines as well as HEK293 cells and HEK293 cells transfected with ADAM17. MED13622 binds equally well to the activated (tumor-associated) and the autoinhibited conformation of ADAM17. The graphs show the C12/MED13622 signal ratio relative to the C12/MED13622 signal ratio observed in the untransfected HEK293 cells. Specifically on the Y axes is plotted the value of.

well as the NSCLC line HCC-827 [54,55], were inhibited to the same extent, with maximum proliferation inhibition of 60 %, observed at a 20 μg/ml concentration of C12 (Fig. 6A). Likewise, the cell-binding experiments indicated that these lines display a comparative, and relatively high, fraction of activated ADAM17 (Fig. 6B). The colon cancer cell (CRC) lines, LIM1215, COLO205, HT-29, HCT116 are dependent for proliferation primarily on Notch signaling, which is mediated by ADAM10 proteinase activity [41,42]. COLO205 contains the $BRAF^{V600E}$ mutation, while HCT116 harbors a mutation in codon 13 of the ras proto-oncogene [56]. Compared to the breast, NSCLC, or ovarian HGSOC and non-HGSOC cell lines, the C12 mAb was less potent in inhibiting to these CRC lines, which was correlated with its lower cell-surface ADAM17-binding affinity. Indeed, here we observed only 28–46 % proliferation inhibition at C12 concentration of 20 μg/ml (Fig. 7A, B). We observed high-degree of correlation between the proliferation inhibition of cancer cells by C12 (at 20 μg/ml concentration) and the fraction of activated ADAM17 on these cancer cells (Fig. S3).

A(C12) / A(MED13622)A(C12-HEK) / A(MED13622-HEK)

where A(C12-HEK) is the signal for C12 using the untransfected HEK293 cells; A(MED13622-HEK) is the signal for MED13622 using the untransfected HEK293 cells; A(C12) is the signal for C12 using the cells that are being evaluated; A(MED13622) is the signal for MED1362 using the cells being evaluated. C12 binds to ADAM17 on HGSOC/non-HGSOC tumors approximately six to seven-fold better than to ADAM17 on HEK2923 cells. However, this preference is diminished (approximately three-fold) in the case of endometroid (TOV112D) cells. The data represent triplicate determinations and two independent experiments, mean ± SEM; $P < 0.001$ by unpaired two-tailed independent t test (cancer cell lines vs HEK293 cells).

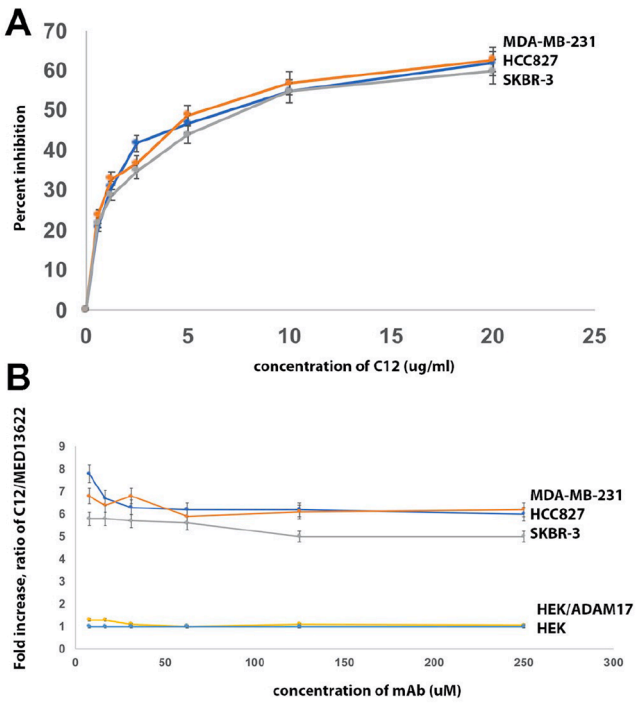


**Fig. 6.** (**A**) Alamar blue cell viability assays with breast and non-small cell lung cancer (NSCLC) cell lines. Percent growth inhibition is shown for breast (MDA-MB-231, SKBR-3) and lung (HCC-827) tumor cell lines treated with C12 IgG. The data represent mean of triplicate determinations and two independent experiments, and the plots show the effect of treatment of mAbs on cancer cells relative to the control, mean ± SEM. (**B**) C12 preferentially binds to the activated, tumor-specific conformation of ADAM17 on breast/NSCLC cells. Cellular ELISA was performed to gauge the binding of C12, relative to the binding of the control MED13622 mAb, to ADAM17 expressed on the cell surface of breast/lung cell lines as well as HEK293 cells and HEK293 cells transfected with ADAM17. C12 binds to ADAM17 on breast and NSCLC-tumors approximately six to eight-fold better than to ADAM17 on HEK293 cells. The data represent triplicate determinations and two independent experiments, mean ± SEM; $P < 0.001$ by unpaired two-tailed independent t test (cancer cell lines vs HEK293 cells).

### *3.7. In vivo anti-tumor potential of C12 mAb in combination with paclitaxel*

Paclitaxel is the most commonly used chemotherapeutic agent for the treatment of ovarian cancer [57]. We used an ovarian cancer xenograft model with SKOV-3 cells to determine the in vivo potency of the C12 mAb alone and in combination with paclitaxel. Early in the treatment, the paclitaxel+C12 mAb arm (after two doses of chemo and four doses of C12 mAb) exhibited 66 % tumor growth inhibition as compared to chemo alone (53 %). The C12 mAb alone showed 37 % tumor growth inhibition (Fig. S4). However, with increasing tumor size the effect wears off. The chemo and the paclitaxel+C12 mAb treatment (after three doses of chemo and eight doses of mAb) resulted in 30 % and 34 % tumor growth inhibition respectively. The C12 mAb alone showed 23 % tumor growth inhibition (Fig. 8A, B). There was no evidence of mAb toxicity in the mice even though C12 binds the mouse ADAM17 equally well as the human protein (Fig. S2)

(Group 1) sterile PBS (as a control, i.p., once a week for 4 weeks).

(Group 2) Paclitaxel (i.v.) 15 mg/kg, three doses, once a week starting day 19.

(Group 3) C12 (i.p.) at a dose of 40 mg/kg, biweekly (total 8 doses) starting day 19.

(Group 4) Paclitaxel (15 mg/kg, i.v., once a week starting day 20, total three doses) + continued C12 mAb treatment (40 mg/kg, i.p., biweekly, total 8 doses, starting day 19).

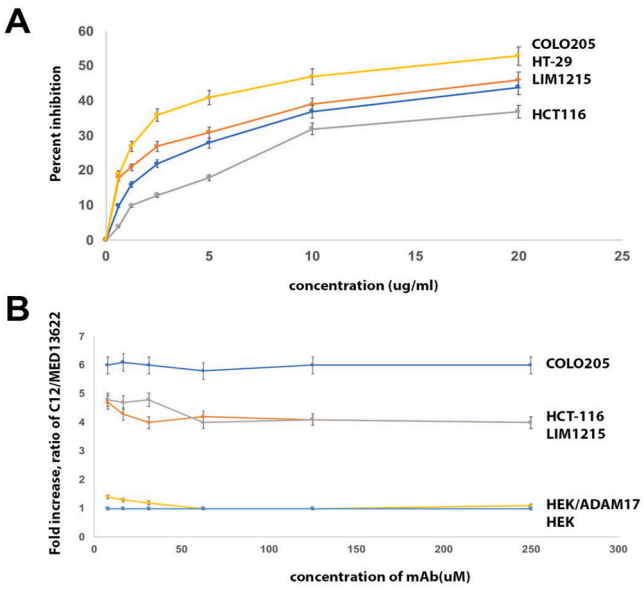


**Fig. 7.** (**A**) Alamar blue cell viability assays with colon cancer cell (CRC) lines. Percent growth inhibition is shown for LIM1215, COLO205, HT-29 and HCT116 tumor cell lines treated with C12 IgG. The data represent mean of triplicate determinations and two independent experiments, and the plots show the effect of treatment of mAbs on cancer cells relative to the control, mean ± SEM. (**B**) C12 preferentially binds to the activated, tumor-specific conformation of ADAM17. Cellular ELISA was performed to gauge the binding of C12, relative to the binding of the control MED13622 mAb, to ADAM17 expressed on the cell surface of CRC lines as well as HEK293 cells and HEK293 cells transfected with ADAM17. C12 binds to ADAM17 on CRC lines approximately four (LIM1215, HCT-116) to six (COLO205) fold better than to ADAM17 on HEK2923 cells. The data represent triplicate determinations and two independent experiments, mean ± SEM; $P < 0.001$ by unpaired two-tailed independent t test (cancer cell lines vs HEK293 cells).

(**A**) Mean tumor volume ± 1 SE from day 19–42. (**B**) In the box and whiskers plot, the black horizontal lines indicate the average value, the top and bottom of the boxes, the interquartile range, and the whiskers, the range.

### 3.8. C12 mAb radiolabeling, PET/CT imaging and biodistribution studies

To examine the in vivo pharmacokinetics and distribution of anti-ADAM17 C12 mAb in vivo, we sought to develop an immunoPET diagnostic radiotracer using zirconium 89, whose physical 3.4 day half-life matched well with the anticipated biological clearance of the mAb. Zr-89 is now an established PET isotope used to track the distribution and in vivo behavior of investigational mAbs and guide therapeutic decisions [58–60]. Accordingly, this strategy was used to trace label C12 with Zr-89 deferoxamine (DFO). The DFO conjugated (DFO-C12 mAb) and $^{89}$Zr radiolabeled ($^{89}$Zr-DFO-C12) mAb were purified by GFC and characterized by radio-SEC HPLC and iTLC. The DFO conjugation (1–2 chelator-to-mAb ratio) and radiometalation had no measurable impact on SEC-HPLC retention time compared to reference standard, and negligible aggregate formation. The iTLC chromatograms indicated that the $^{89}$Zr incorporation was quantitative (Fig. 9). $^{89}$Zr-DFO-C12 was administered IV, then serial micro-PET/CT imaging of tumor-bearing mice was performed at 24-, 72- and 168-hours post-injection. After imaging, ex vivo organ biodistribution was also performed on each cohort to corroborate imaging. The PET/CT data indicated that the C12 mAb performed reasonably well and accumulated in SKOV-3 and OVCAR-3 tumors. $^{89}$Zr-DFO-C12 persisted in blood, gut, and liver extensively, which reflects normal IgG-type distribution, hepatic radiometal residualization or metabolic processing and was expected to some degree considering metalloproteinase biology [39]. Bone uptake is also observed (Fig. 10), which could be a result of metabolically released bone-seeking free Zr-89 metal. It should be noted that undetectable free Zr-89 in the injectate would be removed during purification and $^{89}$Zr-DFO-C12 was stable during storage prior to injection (<6hrs between synthesis and injection). The slow phase of C12 blood clearance was calculated at 14 h ($t_{1/2slow}$) by serial ex vivo blood radioactivity counting at imaging timepoints (Fig. 11A). Quantitation of tumoral region of interest (ROI) and conversion to drug concentration showed C12 reaching a plateau of approximately 35 nM in OVCAR-3 and 10 nM in SKOV-3, which remained reasonably constant after the initial distribution phase before the 24-hour timepoint (Fig. 11B). ROI analysis also indicated that tumor uptake of C12 at 72 h were 6.66±1.84 %ID/g for OVCAR-3 and 2.62±1.52 %ID/g for SKOV-3 tumors, (Fig. 12A). When comparing tumor-to-organ ratios, it is apparent that $^{89}$Zr-DFO-C12 signal is better (higher signal-to-noise) in OVCAR-3 tumors compared to SKOV-3 (Fig. 12 B,C). The differential PET uptake between SKOV-3 and OVCAR-3 was likely a result of slower growth of SKOV-3 at the time of PET imaging (<50 vs 200 mm$^3$), and not due to significantly different expression of activated ADAM17 (Fig. 5B). In a subsequent ex vivo biodistribution study with uniform tumor size (200–300mm$^3$), comparable uptake was observed (Supplementary S5 and S6).

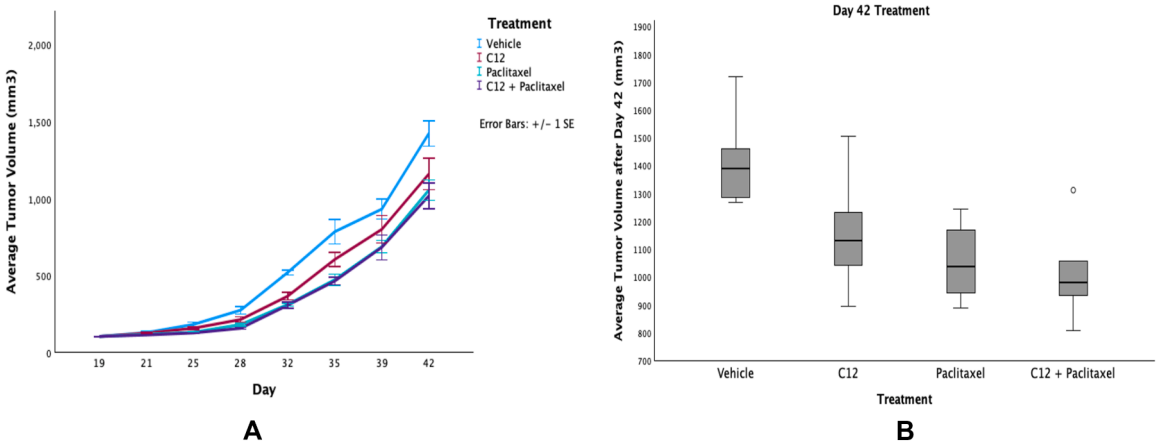


**Fig. 8.** Anti-tumor effect of C12 mAb in an ovarian cancer xenograft model. 6–8 weeks old female NSG mice were used. 10 million SKOV-3 cells per mouse were implanted (subcutaneous with Matrigel). Four groups were used (n=5) for the experiment. When tumor volumes reached ~100 mm3 (day 19 after implantation) the four groups were injected as follows:.

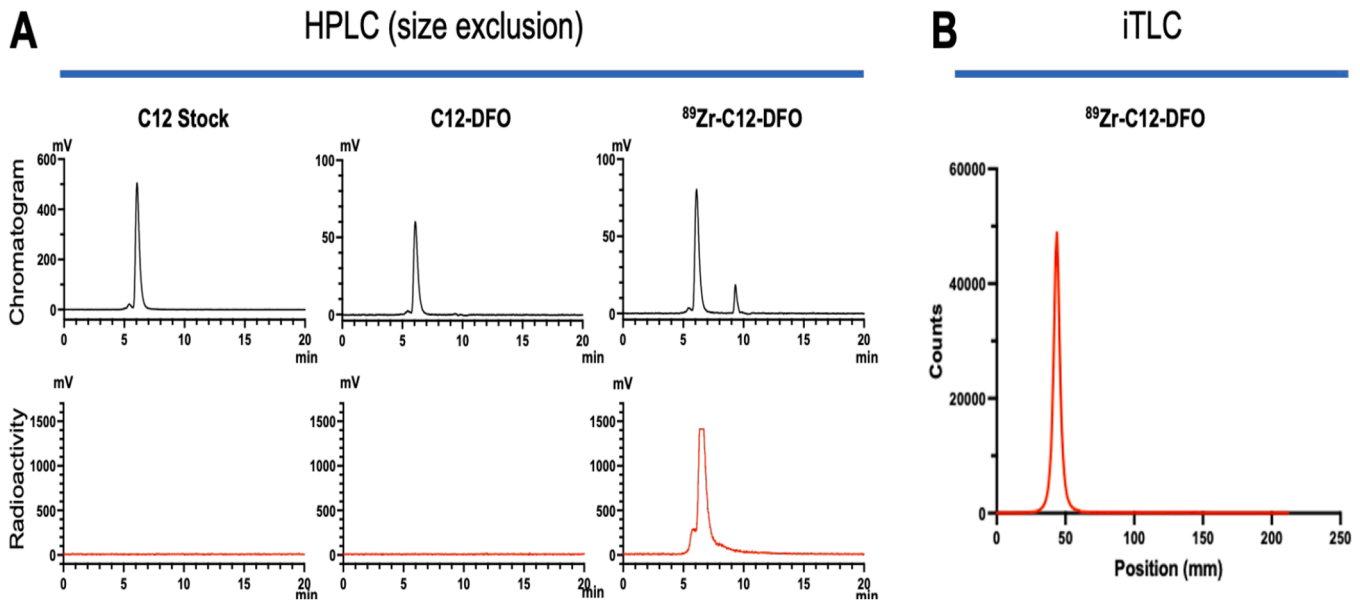


**Fig. 9.** Characterization of $^{89}$Zr-DFO-C12 immunoPET probe Radio-HPLC (SEC) (**A**) and iTLC (**B**) chromatograms. Both SEC and iTLC data demonstrate that $^{89}$Zr radiolabeling was efficient. A) $UV_{280\ nm}$ chromatograms C12 mAb (left), DFO-C12 conjugate (middle) and $^{89}$Zr-DFO-C12 radiotracer (top right) show high chemical purity and molecular weights consistent with GFC standard (data not shown, buffer at 9.4 min). A single radioactive peak for $^{89}$Zr-DFO-C12 was observed (bottom right) indicating high radiochemical purity and an absence of free Zr-89 or unconjugated Zr-89 DFO species. The retention times of DFO conjugated and radiometallated mAbs were nearly identical to the parental mAb, consistent with a low conjugation ratio unlikely to impact mAb binding. The ITLC chromatogram (B) reflects analytically quantitative incorporation of Zr-89 (mAb incorporated Zr-89 peak on left; no free metal peak / $^{89}$Zr-DTPA at solvent front on the right).

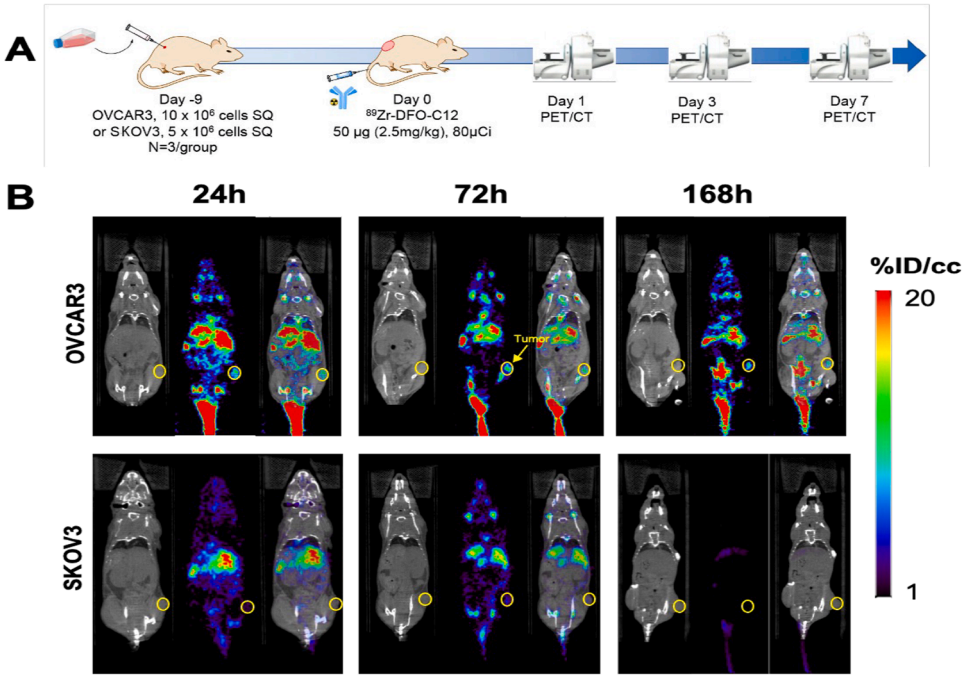


**Fig. 10.** ImmunoPET/CT Imaging of $^{89}$Zr-DFO-C12 anti-ADAM17 in Mouse Models of Human Ovarian Cancer. (**A**) Experimental timeline for PET/CT imaging in NSG mice bearing SKOV-3 or OVCAR-3 flank xenografts. (**B**) Representative coronal images of PET/CT of $^{89}$Zr-DFO-C12 antibody in OVCAR-3 and SKOV-3 xenograft models. $^{89}$Zr-DFO-C12 (50µg, 2.5 mg/kg, $A_M$=1.6 mCi/mg, 80µCi) was administered i.v. by tail vein.

## 4. Discussion

Therapeutic targeting of the ADAM17-mediated signaling pathways, which are implicated in a wide range of solid tumors, including breast, ovarian, lung and prostate, has gained traction [61,62]. To that end, hydroxamate-based small molecule inhibitors that chelate the zinc from the active site of ADAM17, such as the INC class (INCB3619 or the structurally similar INCB7839) and the PF-series (PF-5480090) compounds, inhibit cancer cell proliferation both in vitro and in vivo [13,63,64]. These inhibitors reduce the shedding of EGFR/Her2 ligands, such as TGF alpha, thereby diminishing EGFR activation and phosphorylation [63,64]. In addition to small-molecule inhibitors, inhibitory monoclonal antibodies against ADAM17, namely MED13622, D1A(12) and A9(B8), have also shown promise [65–67]. These mAbs deter the progression of

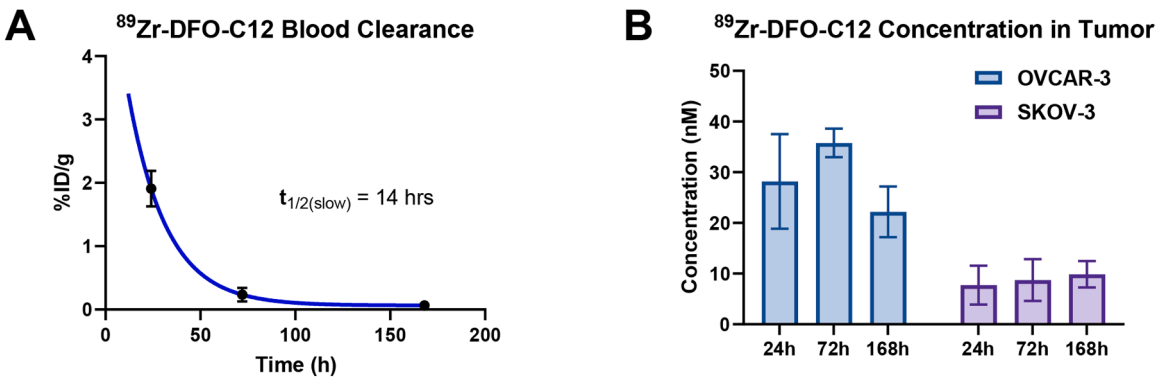


**Fig. 11.** Blood clearance and PET-derived drug accumulation in tumor. (A) Slow phase of blood clearance of $^{89}$Zr-DFO-C12 was $t_{1/2(slow)}$ = 14 hr based on ex vivo blood radioactivity. (B) Tumor concentration (nM) over time based on quantitative PET ROI analysis.

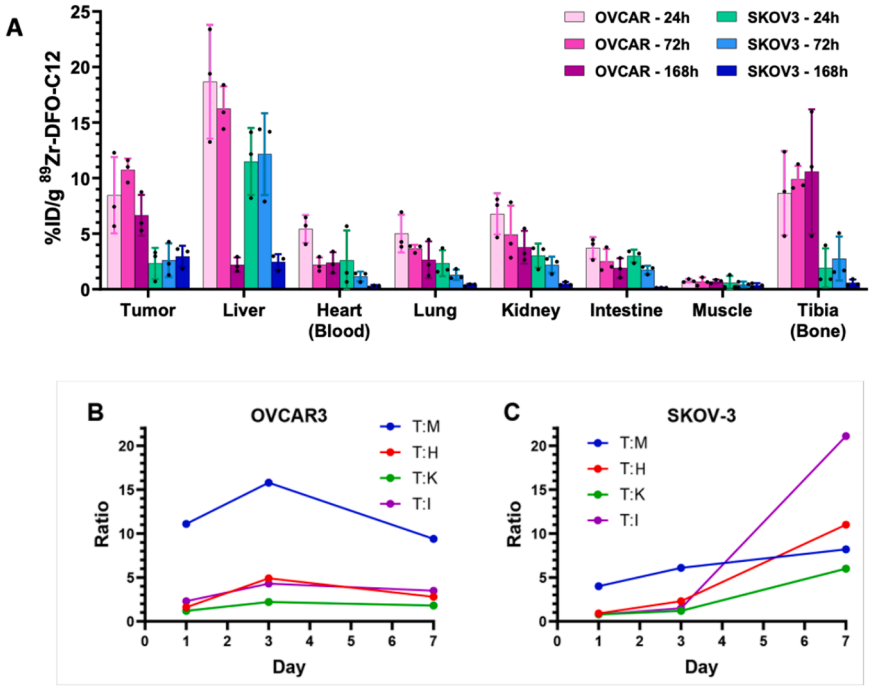


**Fig. 12.** (A) ROI (regions of interest) analysis of $^{89}$Zr-labeled C12 in OVCAR3 and SKOV3 xenograft. $^{89}$Zr-labeled C12 uptake of several organs including tumor were quantified using PET/CT images (n=3 per group, mean±SD). (B,C) Tumor-to-organ ratios. The tumor to organ ratio was derived from ROI data (n=3). T:M tumor to muscle (a measure of general background), H = heart (blood), K = kidney, I = intestine and gut. Lesion detection with $^{89}$Zr-DFO-C12 immuno PET (signal-to-background) was superior in OVCAR-3 compared to SKOV-3.

TNBC, ovarian, NSCLC and prostate cancers in vitro and in preclinical settings. We also previously reported an inhibitory anti-ADAM17 mAb, D8P1C1, which binds the M domain and inhibits its enzymatic activity [16].

Here, we report the generation and characterization of a new anti-ADAM17 mAb, C12, which targets the cysteine-rich domain of ADAM17 and exhibits moderate anti-proliferative effect on an array of cancer cell lines. C12 was more effective in inhibiting the proliferation of breast, NSCLC, HGSOC or non-HGSOC epithelial ovarian cancer lines, as compared to CRC lines. This could be attributed to ADAM17 targeting the EGFR/erbB pathway that drives the progression of breast, NSCLC, and ovarian cancers. Colon cancers, on the other hand, although expressing EGFR/erbB, rely primarily on ADAM10-mediated Notch signaling for progression and metastasis. Similar to our previously described anti-ADAM17 mAb, D8P1C [16], C12 specifically recognizes ADAM17 expressed on cancer cell lines. This suggests that C12 also selectively binds to an activated conformation of ADAM17 prevalent on cancer cells [13,41,42]. Indeed, C12 inhibited better those cell lines that present a higher fraction of activated ADAM17 on their surface (Fig. S3). The binding of C12 to the convex ADAM17 D+C region, away from the MP domain, also explains why C12 does not inhibit the proteolytic cleavage of small peptides, unlike the inhibitory D8P1C1 that directly interacts with the MP domain. Nevertheless, C12 inhibited the shedding of the larger, physiological substrates on the cell surface of a variety of cancer cells. Presumably, the C12 mAb impedes the interaction of ADAM17 (particularly of the substrate-binding D+C region) with such substrates, including EGFR/erbB ligands tethered to either the same or opposing cell (mediating autocrine or juxtacrine signaling, respectively). Consequently, the C12-treated cancer cell lines showed a significant decrease in EGFR/erbB phosphorylation levels.

One of the reasons we are interested in developing inhibitory anti-ADAM antibodies is the involvement of ADAM proteinases in developing resistance to chemotherapy [61,68] suggesting that a combination of chemotherapy with targeted anti-ADAM therapies could prove

beneficial. Overcoming chemoresistance is especially important in ovarian cancer where it evolves in about 70 % of the patients [69] Some recent progress was achieved by introducing Bevacizumab that targets VEGF-A [70] Likewise, OvaRex® (oregovomab), a mAb that binds CA-125, a carbohydrate antigen associated with ovarian cancer, was found to be efficacious [71]. More recently, poly ADP ribose polymerase inhibitors such as Olaparib and Neraparib have given new hope for treating recurrent ovarian cancer [72]. The checkpoint inhibitor Nivolumab is also used to treat epithelial ovarian cancer [73]. Ovarian cancer typically relies on EGFR/erbB signaling, which depends on ADAM17 activity, and we, therefore, evaluated if C12 would act synergistically with chemotherapy using a mouse model. Indeed, in breast cancers that also rely on EGFR/erbB signaling, therapies that involve EGFR/erbB or HER2/erbB2 antagonists (cetuximab and trastuzumab) in combination with chemotherapy, have been approved [74]. Of late, the FDA has also approved the use of antibody-drug conjugates, ado-trastuzumab emtansine and trastuzumab deruxtecan, that target the HER2/erbB2 receptor [75]. For our murine xenograft anti-tumor efficacy evaluation experiments, we chose SKOV-3 cells and performed combination therapy with the chemotherapeutic agent paclitaxel. In epithelial ovarian cancer, taxol-based chemotherapy [57] is known to be the standard first-line of treatment. This preclinical assay showed that C12, in combination with the chemotherapeutic agent paclitaxel, exhibited only moderate efficacy, with the effect tapering off with increasing tumor size. We observed a similar effect with paclitaxel administered alone.

ImmunoPET is underutilized in clinical management of ovarian cancer. $^{89}$Zr-bevacizumab [76] immunoPET has demonstrated utility guiding antiangiogenic therapy in ovarian cancer patients. The diagnostic Zr-89 trastuzumab is a good example of how immunoPET can guide HER2(+) patient selection and therapeutic dosing of T-DM1 in breast cancer [77,78]. However, HER2 targeted approaches have underperformed in gynecological cancer until the recent DESTINY-PanTumor02 Phase II trial which resulted in Trastuzumab deruxtecan (T-DXd) approval for use in ovarian, among other solid cancers in a "pan-tumor" HER2(+) approach [79]. MUC16 is a promising biomarker in ovarian cancer and can be imaged well using Zr-89 immunoPET [80] and in fact, the development of the MUC16xCD3 bispecific ubamatamab (REGN4018) involved immunoPET [81]. There is obvious benefit in developing immunoPET diagnostics as part of evaluating novel ovarian cancer therapeutics. Using anti-ADAM17 immunoPET and organ biodistributions, we show that the anti-ADAM17 mAb C12 targeted human ovarian cancer in two subcutaneous xenograft models (SKOV-3 and OVCAR-3), despite activated ADAM17 being a highly dynamic cell surface target. $^{89}$Zr-DFO-C12 durably accumulated in SKOV3 tumors and has a reasonable rate of blood clearance ($t_{1/2}$ = 14 hrs), somewhat faster than a typical IgG. Enhanced uptake and tumor retention in SKOV3 relative to OVCAR3 indicates that a larger fraction of the ADAM17 pool is activated and surface accessible in SKOV3 [82]. Evidence of internalization and metabolic processing of the $^{89}$Zr-DFO-C12 further justifies activated ADAM17 as a target for antibody and ADC drug development in ovarian cancer [83]. Here, we leveraged this tool to understand the pharmacokinetics and distribution of the anti-ADAM17C12 antibody. Using quantitative PET, the intratumoral drug concentration at a moderate IV tracer dose (2.5 mg/kg) nearly reached the ~30–60 nM (5–10 μg/ml) dose-response plateau observed in in vitro experiments and, thus lends support to the mechanistic hypothesis for the therapeutic effect observed at the 40 mg/kg bi-weekly IP dose of C12. IP administration of a 16-fold higher dose of C12 mAb is likely to far surpass this therapeutic threshold. Imaging and therapy studies taken together, at this dose, the C12 mAb distributes rapidly and extensively, shows no evidence of overt toxicity and is clearly hitting its target. It is tempting to speculate on the potential clinical uses of ADAM17 immunoPET. Noninvasive detection of ADAM17 expression and tumoral activation status is enticing because, like with Zr-89 trastuzumab, one could define which patients are likely to respond to anti-ADAM17 mAb therapy, track antigen escape post-therapy and evaluate ADAM17 as a prognostic biomarker (tumor upregulation or downregulation) in conjunction with conventional chemotherapy, for example.

Finally, given the fact that the C12 mAb: (i) binds to the C-domain of ADAM17 that imparts substrate specificity; (ii) targets an activated conformation of ADAM17 selectively present on cancer cells as opposed to the auto-inhibited conformation present on HEK293 and normal cells; and (iii) accumulates in tumors in PET-based imaging studies, it provides an excellent platform for generating Bispecific T-cell engager antibodies (BiTEs) [84] or CART cells [85] and engage the immune system. These reagents will facilitate targeting and efficient killing of cancer cells without affecting the normal cells and thus pave the way for the treatment of solid tumors such as ovarian, breast and NSCLC.

## CRediT authorship contribution statement

**Nayanendu Saha:** Validation, Methodology, Investigation, Conceptualization. **Kai Xu:** Methodology, Investigation, Data curation. **Yan Xu:** Writing – review & editing, Methodology, Data curation. **Josh Marvald:** Writing – review & editing, Methodology, Data curation. **Tanzy M Love:** Writing – review & editing, Methodology, Data curation. **Elisa de Stanchina:** Supervision, Methodology, Investigation. **Rachelle P. Mendoza:** Software, Methodology, Investigation. **Yehuda Goldgur:** Software, Methodology, Investigation. **Dimitar B. Nikolov:** Writing – original draft, Validation, Project administration, Funding acquisition, Formal analysis, Conceptualization. **M. Jason de la Cruz:** Software, Methodology, Investigation. **Darren Veach:** Writing – original draft, Supervision, Investigation, Funding acquisition, Formal analysis, Data curation. **Eeva-Christine Brockmann:** Software, Methodology, Investigation. **Urpo Lamminmäki:** Writing – review & editing, Methodology, Investigation, Data curation. **Sang Gyu Lee:** Validation, Methodology, Investigation, Data curation. **Juha P. Himanen:** Writing – review & editing, Formal analysis, Data curation.

## Declaration of Competing Interest

The authors declare no conflict of interest.

## Acknowledgements

This work was supported by the Experimental Therapeutics Center of Memorial Sloan-Kettering, support from Mr. William H. and Mrs. Alice Goodwin and the Commonwealth Foundation for Cancer Research to D. B.N., (2023–2024), New York State Spinal Cord Injury Research Program grant (SCIRB funding and DOH-1 Part 5 IDEA award to D.B.N., 2022–2024). and NIH/NCI Cancer Center Support Grant P30 CA008748 to Memorial Sloan Kettering Cancer Center. We also thank the entire staff at New York Structural Biology Center for their excellent support with grid screening and data collection.

## Appendix A. Supporting information

Supplementary data associated with this article can be found in the online version at doi:10.1016/j.biopha.2024.117605.

## References

[1] H.Y.K. Yip, A. Papa, Signaling pathways in cancer: therapeutic targets, combinatorial treatments, and new developments, Cells 10 (3) (2021) 659.
[2] Y. Yarden, M.X. Sliwkowski, Untangling the ErbB signaling network, Nat. Rev. Mol. Cell Biol. 2 (2001) 127–137.
[3] Z. Wang, ErbB receptors and cancer, Methods Mol. Biol. 1652 (2017) 3–35.
[4] D.Y. Oh, Y.J. Bang, HER2-targeted therapies - a role beyond breast cancer, Nat. Rev. Clin. Oncol. 17 (1) (2020) 33–48.
[5] A.E. Cîrstea, A.E. Stepan, C. Mărgăritescu, R.E. Zăvoi, D.A. Olimid, C. E. Simionescu, J. Rom, The immunoexpression of EGFR, HER2 and HER3 in malignant serous ovarian tumors, Morphol. Embryol. 58 (4) (2017) 1269–1273.

[6] M. Riudavets, I. Sullivan, P. Abdayem, D. Planchard, Targeting HER2 in non-small-cell lung cancer (NSCLC): a glimpse of hope? An updated review on therapeutic strategies in NSCLC harbouring HER2 alterations, ESMO Open 6 (5) (2021) 100260.

[7] C.P. Blobel, G. Carpenter, M. Freeman, The role of protease activity in ErbB biology, Exp. Cell Res. 315 (4) (2009) 671–682.

[8] G. Murphy, The ADAMS: signalling scissors in the tumour microenvironment, Nat. Rev. Cancer 8 (2008) 929–941.

[9] M. Drag, G.S. Salvesen, Emerging principles in protease- based drug discovery, Nat. Rev. Drug Discov. 9 (2010) 690–701.

[10] F. Seals, S.A. Courtneidge, The ADAMs family of metalloproteases: multidomain proteins with multiple functions, Genes Dev. 17 (1) (2003) 7–30.

[11] K.M. Smith, A. Gaultier, H. Cousin, D. Alfandari, J.M. White, D.W. Simone, The cysteine-rich domain regulates ADAM protease function in vivo, J. Cell Biol. 159 (5) (2002) 893–902.

[12] P.W. Janes, N. Saha, W.A. Barton, M.V. Kolev, S.H. Wimmer-Kleikamp, E. Nievergall, C.P. Blobel, J.P. Himanen, M. Lackmann, D.B. Nikolov, Adam meets Eph: an ADAM substrate recognition module acts as a molecular switch for ephrin cleavage in trans, Cell 123 (2) (2005) 291–304.

[13] N. Saha, D. Robev, J.P. Himanen, D.B. Nikolov, ADAM proteases: emerging role and targeting of the non-catalytic domains, Cancer Lett. 467 (2019) 50–57.

[14] B. Turk, Targeting proteases: successes, failures, and future prospects, Nat. Rev. Drug Dis. 5 (2006) 785–799.

[15] S. DasGupta, P.R. Murumkar, R. Giridhar, R.M. Yadav, Curr. Perspect. TACE Inhib. A Rev. Bioorg. Med. Chem. 17 (2009) 444–459.

[16] N. Saha, K. Xu, Z. Zhu, D. Robev, T. Kalidindi, Y. Xu, J. Himanen, E. de Stanchina, N.V.K. Pillarsetty, D.S. Dimitrov, D.B. Nikolov, Inhibitory monoclonal antibody targeting ADAM17 expressed on cancer cells, Transl. Oncol. 15 (1) (2022) 101265.

[17] S. Dusterhoft, S. Jung, C.W. Hung, A. Tholey, F.D. Sonnichsen, J. Grotzinger, I. Lorenzen, Membrane-proximal domain of a disintegrin and metalloprotease-17 represents the putative molecular switch of its shedding activity operated by protein-disulfide isomerase, J. Am. Chem. Soc. 135 (2013) 5776–5781.

[18] T.C.M. Seegar, S.C. Blacklow, Domain integration of ADAM family proteins: emerging themes from structural studies, Exp. Biol. Med. 244 (17) (2019), 1510–151.

[19] R.H. Whitehead, F.A. Macrae, D.J. St John, J. Ma, A colon cancer cell line (LIM1215) derived from a patient with inherited nonpolyposis colorectal cancer, J. Natl. Cancer Inst. 74 (4) (1985) 759–765.

[20] T. Huovinen, M. Syrjänpää, H. Sanmark, E.C. Brockmann, A. Azhayev, Q. Wang, M. Vehniäinen, U. Lamminmäki, Two ScFv antibody libraries derived from identical VL-VH framework with different binding site designs display distinct binding profiles, Protein Eng. Des. Sel. 26 (10) (2013) 683–693.

[21] J. O'Brien, I. Wilson, T. Orton, F. Pognan, Investigation of the Alamar Blue (resazurin) fluorescent dye for the assessment of mammalian cytotoxicity, Eur. J. Biochem. 267 (17) (2000) 5421–5426.

[22] P. Primakoff, D.G. Myles, The ADAM gene family: surface proteins with adhesion and protease activity, Trends Genet. 16 (2000) 83–87.

[23] R.A. Black and J.D. Becherer in Tumor Necrosis Factor Alpha -Converting Enzyme. A.J. Barret et al.(eds): Handbook of Proteolytic Enzymes, San Diego: Academic Press, (1998), pp.1315.

[24] D. Smith D, C.B. Cohick, H.B. Lindsley, Optimization of cellular ELISA for assay of surface antigens on human synoviocytes, BioTechniques 22 (1997) 952–957.

[25] J. Rios-Doria, D. Sabol, J. Chesebrough, D. Stewart, L. Xu, R. Tammali, L. Cheng, Q. Du, K. Schifferli, R. Rothstein, C.C. Leow, J. Heidbrink-Thompson, X. Jin, C. Gao, J. Friedman, B. Wilkinson, M. Damschroder, A.J. Pierce, R. E. Hollingsworth, D.A. Tice, E.F. Michelotti, A monoclonal antibody to ADAM17 inhibits tumor growth by inhibiting EGFR and Non-EGFR-mediated pathways, Mol. Cancer Ther. 14 (2015) 1637–1649.

[26] V. Pallarès, D. Calay, L. Cedó, A. Castell-Auví, M. Raes, M. Pinent, A. Ardévol, L. Arola, M. Blay, Enhanced anti-inflammatory effect of resveratrol and EPA in treated endotoxin-activated RAW 264.7 macrophages, Br. J. Nutr. 108 (9) (2012) 1562–1573.

[27] H. Oikawa, C. Maesawa, Y. Tatemichi, Y. Nishinari, M. Nishiya, H. Mizugai, A. Ikeda, K. Oikawa, Y. Takikawa, T. Masuda, A disintegrin and metalloproteinase 17 (ADAM17) mediates epidermal growth factor receptor transactivation by angiotensin II on hepatic stellate cells, Life Sci. 97 (2) (2014) 137–144.

[28] C.S.M. Lee, A. Kaur, S.J. Montague, S.M. Hicks, R.K. Andrews, E.E. Gardiner, Tissue inhibitors of metalloproteinases (TIMPs) modulate platelet ADAM10 activity, Platelets 34 (1) (2023) 2288213.

[29] A.N. Jiang, J.T. Liu, K. Zhao, H. Wu, S. Wang, K. Yan, W. Yang, Specific inhibitor of matrix metalloproteinase decreases tumor invasiveness after radiofrequency ablation in liver tumor animal model, Front Oncol. 10 (2020) 561805.

[30] G.V. Tetering, M. Vooijs, Proteolytic cleavage of notch: hit and run, Curr. Mol. Med. 11 (4) (2011) 255–269.

[31] A. Cheng, E.T. Eng, L. Alink, W.J. Rice, K.D. Jordan, L.Y. Kim, C.S. Potter, B. Carragher, High resolution single particle cryo-electron microscopy using beam-image shift, J. Struct. Biol. 204 (2) (2018) 270–275.

[32] A. Punjani, J.L. Rubinstein, D.J. Fleet, M.A. Brubaker, CryoSPARC: algorithms for rapid unsupervised cryo-EM structure determination, Nat. Methods 14 (3) (2017) 290–296.

[33] E.F. Pettersen, T.D. Goddard, C.C. Huang, G.S. Couch, D.M. Greenblatt, E.C. Meng, T.E. Ferrin, UCSF Chimera - a visualization system for exploratory research and analysis, J. Comput. Chem. 25 (13) (2004) 1605–1612.

[34] J. Zivanov, T. Nakane, B.O. Forsberg, D. Kimanius, W.J.H. Hagen, E. Lindahl, S.H. W. Scheres, New tools for automated high-resolution cryo-EM structure determination in RELION-3, ELife 7 (2018) 1–22.

[35] J. Leem, J. Dunbar, G. Georges, J. Shi, C.M. Deane, ABodyBuilder: automated antibody structure prediction with data–driven accuracy estimation, MAbs 8 (2016) 1259–1268.

[36] P.V. Afonine, R.W. Grosse-Kunstleve, N. Echols, J.J. Headd, N.W. Moriarty, M. Mustyakimov, T.C. Terwilliger, A. Urzhumtsev, P.H. Zwart, P.D. Adams, Towards automated crystallographic structure refinement with phenix Refine, Acta Cryst. D. 68 (2012) 352–367.

[37] T.A. Jones, J.Y. Zou, S.W. Cowan, and M. Kjeldgaard. Improved Methods for Building Protein Models in Electron Density Maps and the Location of Errors in These Models (1991) Acta Crystallogr., A 47: (1991), pp. 110–119.

[38] J.J. Headd, N. Echols, P.V. Afonine, R.W. Grosse-Kunstleve, V.B. Chen, N. W. Moriarty, D.C. Richardson, J.S. Richardson, P.D. Adams, Use of knowledge-based restraints in phenix.refine to improve macromolecular refinement at low resolution, Acta Cryst. D 68 (2012) 381–390.

[39] M.J. Vosjan, L.R. Pderk, G.W. Visser, M. Budde, P. Jurek, G.E. Keifer, G. A. VanDongan, Conjugation and radiolabeling of monoclonal antibodies with zirconium-89 for PET imaging using the bifunctional chelate p-isothiocyanatobenzyl-desferrioxamine, Nat. Protoc. 5 (4) (2010) 739–743.

[40] A.M. Loening, S.S. Gambhir, AMIDE: a free software tool for multimodality medical image analysis, Mol. Imaging 2 (3) (2003) 131–137, 2003.

[41] N. Saha, D.S. Baek, R.P. Mendoza, D. Robev, Y. Xu, Y. Goldgur, M.J. de la Cruz, E. deStanchina, P.W. Janes PW, K. Xu, D.S. Dimitrov, D.B. Nikolov, Fully human monoclonal antibody targeting activated ADAM10 on colorectal cancer cells, Biomed. Pharmacother. 161 (2023) 11494.

[42] L. Atapattu, N. Saha, C. Chheang, M.F. Eissman, K. Xu, M.E. Vail, L. Hi, C. Llerena, Z. Liu, K. Horvay, H.E. Abud, U. Kusebauch, R.L. Moritz, B.S. Ding, Z. Cao, S. Rafii, M. Ernst, A.M. Scott, D.B. Nikolov, M. Lackman, P.W. Janes, An activated form of ADAM10 is tumor selective and regulates cancer stem-like cells and tumor growth, J. Exp. Med. 213 (9) (2016) 1741–1757.

[43] F.F. Lu, H. Zhao, Y. Dai, Y. Wang, C.H. Lee, M. Freeman, Cryo-EM reveals that iRhom2 restrains ADAM17 protease activity to control the release of growth factor and inflammatory signals, Mol. Cell 84 (11) (2024) 2152–2165.

[44] O. Giricz, V. Calvo, E.A. Peterson, C.M. Abouzeid, P.A. Kenny, TACE-dependent TGF-alpha shedding drives triple-negative breast cancer cell invasion, Int. J. Cancer 133 (11) (2013) 2587–2595.

[45] J.T. Price, T. Tiganis, A. Agarwal, D. Djakiew, E.W. Thompsom, Epidermal growth factor promotes MDA-MB-231 breast cancer cell migration through a Phosphatidylinositol 3′-Kinase and phospholipase C-dependent mechanism, Cancer Res. 59 (21) (1999) 5475–5478.

[46] L. Zhou, B.S. Leung, Growth regulation of ovarian cancer cells by epidermal growth factor and transforming growth factors alpha and beta 1, Biochim. Biophys. Acta 1180 (2) (1992) 130–136.

[47] J. Ebott, J. McAdams, C. Kim, C. Jansen, M. Woodman, P.D.La Cruz, C. Schrol, J. Ribeiro, N. James, Enhanced amphiregulin exposure promotes modulation of the high grade serous ovarian cancer tumor immune microenvironment, Front. Pharmacol. 15 (2024) 1375421.

[48] H. Narasimhan, F. Ferraro, A. Bleilevens, R. Weiskirchen, E. Stickeler, J. Maurer, Tumor Necrosis Factor-α (TNFα) stimulate triple-negative breast cancer stem cells to promote intratumoral invasion and neovasculogenesis in the liver of a xenograft model, Biology 11 (10) (2022) 1481.

[49] C. Zhao, Y. Gao, P. Ding, T. Wu, G. Ji, The role of CXCL family members in different diseases, Cell Death Discov. 9 (1) (2023). Article. 212.

[50] G. van Tetering, P. van Diest, I. Verlaan, E. van der Wall, R. Kopan, M. Vooijs, Metalloprotease ADAM10 is required for notch1 Site 2 cleavage, J. Biol. Chem. 284 (45) (2009) 31018–31027.

[51] P.O. Hackel, E. Zwick, N. Prenzel, A. Ullrich, Epidermal growth factor receptors: critical mediators of multiple receptor pathways, Curr. Opin. Cell. Biol. 11 (2) (1999) 184–189.

[52] E. Zwick, P.O. Hackel, N. Prenzel, A. Ullrich, The EGF receptor as central transducer of heterologous signaling systems, Trends Pharmacol. Sci. 20 (10) (1999) 408–412.

[53] P. Ramalingam, Morphologic, immunophenotypic, and molecular features of epithelial ovarian cancer, Oncology 30 (2) (2016) 166–176.

[54] O. Giricz, V. Calvo, E.A. Peterson, C.M. Abouzeid, P.A. Keny, TACE-dependent TGF-alpha shedding drives triple-negative breast cancer cell invasion, Int. J. Cancer 133 (11) (2013) 2587–2595.

[55] K. Subik, J.F. Lee, L. Baxter, T. Strzepek, D. Costello, L. Xing, M.C. Hung, T. Bonfiglio, D.G. Hicks, P. Tang, The Expression Patterns of ER, PR, HER2, CK5/6, EGFR, Ki-67 and AR by immunohistochemical analysis in breast cancer cell lines, Breast Cancer 4 (2010) 35–41.

[56] S. Pal, V.B. Konkimalla, L. Kathawate, S. Rao, Targeting a chemo refractory COLO205 (BRAF V600E) cell line using substituted benzo[α]phenoxazines, RCS Adv. 5 (2015) 82549–82563.

[57] G.S. Huang, L.L. Barcons, S. Freeze, A.B. Smith III, G.L. Goldberg, S. BandHorwitz, H.M. McDaid, Potentiation of Taxol efficacy by discodermolide in ovarian carcinoma xenograft-bearing mice, Clin. Cancer Res. 12 (1) (2006) 298–304.

[58] J.K. Yoon, B.N. Park, E.K. Ryu, Y.S. An, S.J. Lee, Current perspectives on $^{89}$Zr-PET imaging, Int. J. Mol. Sci. 21 (12) (2020) 4309.

[59] G.A. Ulaner, D.M. Hyman, S.K. Lyashchenko, J.S. Lewis, J.A. Carrasquillo, 89Zr-Trastuzumab PET/CT for detection of human epidermal growth factor receptor 2-positive metastases in patients with human epidermal growth factor receptor 2-negative primary breast cancer, Clin. Nucl. Med. 42 (12) (2017) 912–917.

[60] F. Bensch, A.H. Brouwers, M.N. Lub-de Hooge, J.R. de Jong, B. van der Vegt, S. Sleijfer, E.G.E. de Vries, C.P. Schröder, $^{89}$Zr-trastuzumab PET supports clinical decision making in breast cancer patients, when HER2 status cannot be determined by standard work up, Eur. J. Nucl. Med. Mol. Imaging 45 (13) (2018) 2300–2306.

[61] N. Hedemann, C. Rogmans, S. Sebens, D. Wesch, M. Reichert. ADAM17 Inhibition Enhances Platinum Efficiency in Ovarian Cancer, Oncotarget. Vol (9): (2018), pp. 16043-16058.
[62] P.M. McGowan, M. Mullooly, F. Caiazza, S. Sukor, S.F. Madden, A.A. Maguire, A. Pierce, E.W. McDermott, J. Crown, N. O'Donovan, M.J. Duffy, ADAM-17: a novel therapeutic target for triple negative breast cancer, AnnOncol (2) (2013) 362–369.
[63] L. Witters, P. Scherle, S. Friedman, J. Fridman, E. Caulder, R. Newton, A. Lipton, Synergistic inhibiton with a dual epidermal growth factor receptor/ HER-2/ neu tyrosine kinase inhibitor and a disintegrin and metalloprotease inhibitor, Can. Res. 68 (17) (2008) 7083–7089.
[64] R.C. Newton, E.C. Bradley, R.S. Levy, D. Doval, S. Bondarde, T.P. Sahoo, D. Lokanatha, P.K. Julka, R. Nagarkar, S.M. Fridman, Targeting ADAM-mediated ligand cleavage to inhibit HER2 and EGFR pathways in non-small cell lung cancer, Cancer Cell 10 (1) (2006) 39–50.
[65] F.M. Richards, C.J. Tape, D.I. Jodrell, G. Murphy, Anti-tumour effects of a specific anti-ADAM17 antibody in an ovarian cancer model in vivo, PLoS One 7 (7) (2012) e40597.
[66] C.J. Tape, S.H. Willems, S.L. Dombernowsky, P.L. Stanley, M. Fogarasi, W. Ouwehand, J. McCafferty, G. Murphy, Cross-domain inhibition of TACE ectodomain, Proc. Natl. Acad. Sci. USA 108 (14) (2011) 5578–5583.
[67] Y. Huang, N. Benaich, C. Tape, H.F. Kwok, G. Murphy, Targeting the sheddase activity of ADAM17 by an anti-ADAM17 antibody D1 (A12) inhibits head and neck squamous cell carcinoma cell proliferation and motility via blockage of bradykinin induced HERs transactivation, Int. J. Biol. Sci. 10 (2014) 702–714.
[68] G. Hugendieck, M. Lettau, S. Andreas, S. Neuman, N. Reinhardt, et al., Chemotherapy-induced release of ADAM17 bearing EV as a potential resistance mechanism in ovarian cancer. J. Extra Vesic. 12 (7) (2023) 12338.
[69] K. Brasseur, N. Gévry, E. Asselin, Chemoresistance and targeted therapies in ovarian and endometrial cancers, Oncotarget 8 (3) (2017) 4008–4042.
[70] C.L. Mao, K.M. Seow, K.H. Chen, The utilization of Bevacizumab in patients with advanced ovarian cancer: a systematic review of the mechanisms and effects, Int J. Mol. Sci. 23 (13) (2022) 6911.
[71] A. Chandra, C. Pius C, M. Nabeel, M. Nair, J.K. Vishwnatha, S. Ahmad, R. Basha, Ovarian cancer: current status and strategies for improving therapeutic outcomes, Cancer Med. 8 (16) (2019) 7018–7031.
[72] M.W. Wong-Brown, A. van der Westhuizen, N.A. Bowden, Targeting DNA repair in ovarian cancer treatment resistance, Clin. Oncol. 32 (2020) 518–526.
[73] B.A. Maiorano, M.F.P. Maiorano, D. Lorusso, E. Maiello, Ovarian cancer in the era of immune checkpoint inhibitors: state of the art and future perspectives, Cancers 13 (17) (2021) 4438.
[74] N. O'Donovan, J. Crown, EGFR and HER-2 antagonists in breast cancer, Anticancer Res. 27 (2007) 1285–1294.
[75] E. Rassy, L. Rached, B. Pistilli, Antibody drug conjugates targeting HER2: clinical development in metastatic breast cancer, Breast 66 (2022) 217–226.
[76] A.R.M. van der Bilt, A.G.T.T. van Scheltinga, H.T. Bosscha, C.P. Schröder, L. Pot, J. G.W. Kosterink, A.G.J. van der Zee, M.N. Lub-de Hooge, S. de Jong, E.G. De Vries, A.K.L. Reyners, Measurement of tumor VEGF-A levels with 89Zr-bevacizumab PET as an early biomarker for the antiangiogenic effect of everolimus treatment in an ovarian cancer xenograft model, Clin. Cancer Res. 18 (22) (2012) 6306–6314.
[77] J. Capala, K. Bouchelouche, Molecular imaging of HER2-positive breast cancer: a step toward an individualized 'image and treat' strategy, Curr. Opin. Oncol. 22 (6) (2010) 559–566.
[78] G. Gebhart, L.E. Lamberts, Z. Wimana, C. Garcia, P. Emonts, L. Ameye, S. Stroobants, M. Huizing, P. Aftimos, J. Tol, W.J.G. Oyen, D.J. Vugts, O. S. Hoekstra, C.P. Schröder, C.W. Menke-van der Houven van Oordt, T. Guiot, A. H. Brouwers, A. Awada, E.G.E. de Vries, P. Flamen, Molecular imaging as a tool to investigate heterogeneity of advanced HER2-positive breast cancer and to predict patient outcome under trastuzumab emtansine (T-DM1): the ZEPHIR trial, J. Clin. Oncol. 27 (4) (2016) 619–624.
[79] F.M. Bernstam, V. Makker, A. Oaknin, D.Y. Oh, S. Banerjee, A.G. Martín, K.H. Jung, I. Ługowska, L. Manso, A. Manzano, B. Melichar, S. Siena, D. Stroyakovskiy, A. Fielding, Y. Ma, S. Puvvada, N. Shire, J.Y. Lee, Efficacy and safety of Trastuzumab Deruxtecan in patients with HER2-expressing solid tumors: primary results from the DESTINY-PanTumor02 phase II Trial, J. Clin. Oncol. 42 (1) (2024) 47–58.
[80] S.K. Sharma, K.N. Mack, A. Piersigilli, J. Pourat, K.J. Edwards, O. Keinänen, M. S. Jiao, H. Zhao, B. White, C.L. Brooks, E. deStanchina, M.R. Madiyalakan, M. A. Hollingsworth, P. Radhakrishnan, J.S. Lewis, B.M. Zeglis, ImmunoPET of ovarian and pancreatic cancer with AR9.6, a novel MUC16-targeted therapeutic antibody, Clin. Cancer Res. 28 (5) (2022) 948–959.
[81] A. Crawford, L. Haber, M.P. Kelly, K. Vazzana, L. Canova, P. Ram, A. Pawashe, J. Finney, S. Jalal, D. Chiu, C.A. Colleton, E. Garnova, S. Makonnen, C. Hickey, P. Krueger, F. DelFino, T. Potocky, J. Kuhnert, S. Godin, M.W. Retter, P. Duramad, D. MacDonald, W.C. Olson, J. Fairhurst, T. Huang, J. Martin, J.C. Lin, E. Smith, G. Thurston, J.R. Kirshner, A Mucin 16 bispecific T cell-engaging antibody for the treatment of ovarian cancer, Sci. Transl. Med. 11 (497) (2019) eaau7534.
[82] L. Thouvenin, M. Charrier, S. Clement Y.Christinat, J.C. Tille, M.Frigeri K. Homicsko, O. Michielin, A. Bodmer, P.O. Chappuis, T.A. McKee, P. Tsantoulis, Ovarian cancer with high-level focal ERBB2 amplification responds to trastuzumab and pertuzumab, Gynecol. Oncol. Rep. 37 (2021) 100787.
[83] J.A. Flygare, T.H. Pillow, P. Aristoff, Antibody drug conjugates for the treatment of cancer, Chem. Biol. Drug Des. 81 (2013) 113–121.
[84] P.A. Baeuerle, C. Reinhardt, Bispecific T-cell engaging antibodies for cancer therapy, Cancer Res. 69 (2009) 4941–4944.
[85] L. Labanieh, R.G. Majzner, C.L. Mackall, Programming CAR-T cells to kill cancer, Nat. Biomed. Eng. 2 (6) (2018) 377–391.